On the mechanical properties of dual-scale microlattice of starfish ossicles: a computational study

Hongshun Chen[1], Zian Jia[1], Zhifei Deng[1], Ling Li*

Affiliation
[1]Department of Mechanical Engineering, Virginia Tech, Blacksburg, VA 24060, USA.

Author for correspondence: Ling Li. E-mail: lingl@vt.edu.

Abstract

While engineering cellular solids, either stochastic foams or architected lattices, are usually made of polycrystalline or amorphous materials, echinoderms (e.g., sea urchins, starfish, and brittle stars) build their microporous skeletal elements with single-crystalline calcite. This class of biomineralized cellular solid, known as stereom, also exhibits a vast diversity in pore morphology, ranging from random open-cell foams to fully periodic lattices. In particular, the skeletal elements of some starfish species, known as ossicles, are composed of a diamond-triply periodic minimal surface (diamond-TPMS) microlattice. In addition, the crystallographic symmetries at both atomic (calcite) and lattice (diamond-TPMS) levels are precisely aligned. Here we investigate the mechanical performance of this unique dual-scale microlattice and discuss the synergistic effects of atomic- and lattice-scale crystallographic coalignment. Our computational and theoretical analysis suggests that the mechanical isotropy of ossicles is significantly enhanced due to the property compensation between the atomic-level and lattice-level architectures. Moreover, the observed 50 vol% relative density in the diamond-TPMS microlattice of ossicles may be a result of achieving overall mechanical isotropy, minimal surface curvature, and maximized surface area. We believe the methodology introduced here will be useful for understanding the mechanical behavior of natural crystalline cellular solids such as echinoderms' stereom and designing dual-scale lattice materials.

Keywords: Dual-scale coalignment, starfish ossicles, biomineral, mechanical properties, architected lattice

1. Introduction

Recent advancement of additive manufacturing has enabled the fabrication of 3D architected lattice materials from a variety of polymers, metals, ceramics/glass, or composites [1–3]. These architected lattices may exhibit some unusual mechanical properties, such as isotropic elastic stiffness approaching theoretical limits, negative Poisson's ratios, and etc [1,3–9]. The introduction of hierarchical designs further expands the material property space by tailoring mechanical behaviors at different length scales [10–13]. For example, one strategy to introduce structural hierarchy of architected lattices is to design the branches into cellular architectures at a smaller length scale [2,10–13]. Another is to engineer the material-level design of the branches, including core-shell composites, fiber- and particle-reinforced composites, high-entropy alloy with crystallographic texture, and etc [14–22]. However, single-crystalline constituent at atomic scale has rarely been taken into consideration for the mechanical design of hierarchical lattices.

Unlike artificial architected lattices that are typically composed of polycrystalline or amorphous constituents, the porous, biomineralized skeletal elements of many echinoderms (e.g., starfish, sea urchins, and brittle star) is composed of calcite that often diffracts as a single crystal [23–26]. This type of biological cellular solids, known as stereom, exhibits a vast diversity in pore morphology, ranging from random open-cell foams to fully periodic lattices [27]. While significant research efforts have been made to correlate the crystallographic orientation of calcite with the orientation of skeletal elements, such as the test (shell) plates and spines of sea urchins [23,25,26,28], how the calcite's crystallographic orientations are aligned with the local pore morphology and organization in stereoms remains largely unknown [29–32].

Recently, our group has demonstrated that the skeletal elements (known as ossicles) of certain starfish species (e.g., *Protoreaster nodosus*) are composed of a diamond-triply periodic minimal surface (diamond-TPMS) microlattice (relative density, $\bar{\rho}$, ~50 vol%) [33]. In this natural architected microlattice, the crystallographic symmetries at both atomic (calcite, space group $R\bar{3}c$) and lattice (diamond, space group $Fd\bar{3}m$) levels are precisely aligned [33]. Specifically, the c-axis of calcite coincides with the $[111]$ direction of the diamond-TPMS microlattice, which is also along the normal direction of the animal (e.g., from oral to aboral sides of starfish) [33]. Meanwhile, the $[4\bar{4}0\bar{1}]$, $[04\bar{4}\bar{1}]$ and $[\bar{4}04\bar{1}]$ directions of calcite (the directions formed by the intersection of two adjacent $\{10\bar{1}4\}$ cleavage planes) are approximately aligned with the directions of non-$[111]$ branches (i.e., $[1\bar{1}\bar{1}]$, $[\bar{1}1\bar{1}]$ and $[\bar{1}\bar{1}1]$-branches, respectively) of the tetrahedron unit cell in diamond-TPMS lattice [33], through which the in-plane three-fold symmetry between calcite (plane perpendicular to c-axis or $[0001]$ direction) and diamond lattice ((111) plane) are precisely registered.

While our previous analysis suggests that this dual-scale crystallographic coalignment in ossicles may provide a stiffness compensation for selected crystallographic directions, we lack a full understanding of the 3D mechanical properties of starfish ossicles [33,34]. Here we develop a combined computational and theoretical methodology for predicting the 3D elastic properties of the dual-scale architected lattices with crystallographic coalignment. Furthermore, by analyzing the mechanical isotropy, strength, and structure of the dual-scale diamond-TPMS microlattice, we provide insights for the formation of starfish ossicles (e.g., why particular relative density and dual-scale coalignment are selected).

2. Methods

2.1. Model system and modeling

Here, the model system investigated is a dual-scale diamond-TPMS lattice as observed in the biomineralized stereom structure found in the ossicles of starfish *P. nodosus* [33]. This type of stereom has been found to possess a diamond-TPMS microlattice structure made of single-crystalline biogenic calcite, which was demonstrated by micro-computed tomography (μ-CT) analysis, scanning electron microscopy

(SEM) imaging (**Fig. 1a-e**), and epitaxial overgrowth of calcite (**Fig. 1f,g**). The crystallographic orientations of the constituent calcite and the diamond microlattice have a specific coalignment, resulting in a so-called dual-scaled coalignment structure (**Fig. 1g**) [33] (see detailed structural introduction in section 3.1). To generate models for mechanical investigation, we constructed diamond-TPMS structures of several different types.

Firstly, the diamond-TPMS structure's iso-surface (U) is generated by Eq. (1):

$$U = S_{x_0}S_{y_0}S_{z_0} + S_{x_0}C_{y_0}C_{z_0} + C_{x_0}S_{y_0}C_{z_0} + C_{x_0}C_{y_0}S_{z_0} - T \quad (1),$$

where $S_i = sin\,(k_i \cdot i)$, $C_i = cos\,(k_i \cdot i)$, and $i = x_0, y_0, or\ z_0$ represent three orthogonal directions of the Cartesian coordinates, corresponding to $[100]$, $[010]$, and $[001]$ directions of the diamond-TPMS microlattice, respectively. $k_i = 2\pi n_i/L_i$ is defined as the periodicity, where n_i and L_i represent the number of cells and the size of the diamond-TPMS structure along the x_0, y_0 and z_0 directions, respectively. T is a geometric parameter that controls the relative density of the diamond-TPMS structure [35]. The solid region enclosed by $U < 0$ was chosen to generate a diamond-TPMS lattice, while various T was chosen (-0.5, -0.25, 0, 0.25, and 0.5) to produce microlattice with various relative densities $\bar{\rho}$ (30%, 40%, 50%, 60%, and 70%).

Secondly, four different models were constructed for mechanical simulations and comparisons, including the constituent solid calcite, diamond-TPMS microlattice with equivalent isotropic calcite (I-dTPMS), dual-scale diamond-TPMS microlattices (DS-dTPMS) as observed in starfish ossicles, and DS-dTPMS (180°) which is a modified DS-dTPMS with calcite rotated 180° about its c-axis (**Fig. 2a**). The material property inputs (i.e., equivalent isotropic and anisotropic calcites, respectively) were illustrated along with the simulation method later (**Table S1**). To build the DS-dTPMS, the diamond-TPMS microlattice generated using Eq. (1) was first rotated to a new coordinate system with three principal directions of $[1\bar{1}0]$, $[11\bar{2}]$, and $[111]$. These directions correspond to the $[1\bar{2}10]$, $[10\bar{1}0]$, and $[0001]$ directions of calcite as observed in the ossicles, respectively [36,37]. We further denote these three directions as 1, 2, and 3 directions. Therefore, DS-dTPMS (180°) has $[1\bar{1}0]$ and $[11\bar{2}]$ directions of the diamond-TPMS microlattice aligned with the $[\bar{1}2\bar{1}0]$ and $[\bar{1}010]$ directions of calcite, respectively. The representative volume elements (RVE) of diamond-TPMS microlattice based on these configurations measure 49.0 μm, 42.4 μm, and 60.0 μm along $[1\bar{1}0]$, $[11\bar{2}]$, and $[111]$ directions, respectively, where the branch length was set 15.0 μm, following the previous measurement of starfish ossicles (**Fig. S1a**) [33].

2.2. Structural analysis

Structural analyses, including 3D Fast Fourier Transform (3D-FFT) analysis, surface curvature analysis, and surface area analysis, were performed on representative cubic volumes of ossicles and the generated diamond-TPMS microlattices, respectively.

3D Fast Fourier Transform (3D-FFT) analysis was performed on the 3D binary data of cubic volumes of ossicles using the 3D-FFT module in Avizo 2019.2 (Thermo Fisher Scientific. MA, USA). The 3D logarithmic plot of the 3D-FFT data was used for visualization [33].

A customized Python script was developed to generate the binary image slices of the diamond-TPMS microlattice obtained from Eq. (1), which were subsequently fed to Avizo to generate corresponding Standard Triangle Language (STL) models. These STL models were used for surface curvature analysis and surface-area-to-volume ratio (SAV) calculations. The surface curvature analysis module in Avizo was used to obtain the principal curvatures, i.e., minimum and maximum curvatures (κ_1 and κ_2). The mean surface curvature, H, of each node was calculated using $H = (\kappa_1 + \kappa_2)/2$. The interfacial shape distribution (ISD) of κ_1 versus κ_2 was plotted using OriginPro 2016 (OriginLab. MA, USA). SAV is

calculated by dividing the total surface area of a unit cell (A) of the diamond-TPMS microlattices by the total volume of the unit cell (i.e., the volume occupied by the unit cell, V) as:

$$SAV = \frac{A}{V} \quad (2).$$

Therefore, SAV is dependent on the unit cell size and the unit for SAV is the inverse of the unit of length (i.e., μm^{-1}).

2.3. 3D elastic property prediction workflow

As described in section 2.1, the constituent solid calcite and various diamond-TPMS models were constructed for mechanical comparison (**Fig. 2a**). To predict the 3D elastic properties of these models, a four-step workflow was proposed (**Fig. 2b**): (1) configurations of material properties and periodic boundary conditions (PBCs) for FE simulations on all diamond-TPMS models with imposed compressive strain such as ε_{33} and shear strain such as γ_{23}, (2) computational simulations of the full stiffness matrix of the diamond-TPMS models, (3) transformations of the full stiffness matrix obtained from simulations to calculate elastic properties in any arbitrary 3D directions, and (4) visualization of the 3D elastic property based on the calculated directional elastic properties. The detailed workflow of simulations and calculations were introduced as follows.

Finite element (FE) simulations: To obtain the full stiffness matrix of the diamond-TPMS microlattices, we utilized Abaqus/Standard 2016 (Dassault Systems, Vélizy-Villacoublay, France) to perform static mechanical simulations, including uniaxial and shear loadings, on the RVEs of diamond-TPMS microlattice with PBCs (**Fig. S1b-d**).

The RVEs for I-dTPMS, DS-dTPMS, and DS-dTPMS (180°) all contained ca. 3 million linear tetrahedral elements (C3D4). To evaluate the effects of mechanical anisotropy at constituent material level, anisotropic and equivalent isotropic calcite properties were used as material input. For DS-dTPMS and DS-dTPMS (180°), the full stiffness matrix of single-crystalline calcite was used:

$$C^{Calcite} = \begin{pmatrix} c_{11} & c_{12} & c_{13} & c_{14} & 0 & 0 \\ c_{12} & c_{11} & c_{13} & -c_{14} & 0 & 0 \\ c_{13} & c_{13} & c_{33} & 0 & 0 & 0 \\ c_{14} & -c_{14} & 0 & c_{44} & 0 & 0 \\ 0 & 0 & 0 & 0 & c_{44} & c_{14} \\ 0 & 0 & 0 & 0 & c_{14} & c_{66} \end{pmatrix} \quad (3).$$

Each stiffness coefficient $c_{MN}^{Calcite}$ ($M, N = 1-6$ in Voigt notations where $4 \rightarrow 23$, $5 \rightarrow 13$, and $6 \rightarrow 12$) is given in **Table S1** [37]. For I-dTPMS, the equivalent isotropic material properties of calcite (elastic modulus $E_{Equivalent}^{Calcite} = 109\ GPa$, Poisson's ratio $v_{Equivalent}^{Calcite} = 0.29$) was used [37].

Six types of mechanical loadings, including compression in 1, 2, and 3 directions, and pure shear in 4, 5, and 6 directions with a strain of 0.1% were applied on the RVEs (**Fig. 2b**). Subsequently, the obtained stress-strain relationships from the simulations were used to calculate all stiffness coefficients of the diamond-TPMS microlattices. Due to the trigonal symmetry, the stiffness matrices for I-dTPMS, DS-dTPMS, and DS-dTPMS (180°) in the orthogonal system with bases of $[1\bar{1}0]$, $[11\bar{2}]$, and $[111]$ share the same form as following:

$$C^{I/DS-dTPMS} = \quad (4)$$

.

$$\begin{pmatrix} c_{11}^{I/DS-dTPMS} & c_{12}^{I/DS-dTPMS} & c_{13}^{I/DS-dTPMS} & c_{14}^{I/DS-dTPMS} & 0 & 0 \\ c_{12}^{I/DS-dTPMS} & c_{11}^{I/DS-dTPMS} & c_{13}^{I/DS-dTPMS} & -c_{14}^{I/DS-dTPMS} & 0 & 0 \\ c_{13}^{I/DS-dTPMS} & c_{13}^{I/DS-dTPMS} & c_{33}^{I/DS-dTPMS} & 0 & 0 & 0 \\ c_{14}^{I/DS-dTPMS} & -c_{14}^{I/DS-dTPMS} & 0 & c_{44}^{I/DS-dTPMS} & c_{44}^{I/DS-dTPMS} & c_{14}^{I/DS-dTPMS} \\ 0 & 0 & 0 & 0 & c_{14}^{I/DS-dTPMS} & c_{66}^{I/DS-\ \ TPMS} \\ 0 & 0 & 0 & 0 & & \end{pmatrix}$$

PBCs were used in all simulations, as shown in **Fig. S1b-d**. The PBCs are imposed on the opposite surfaces, edges, and vertices, separately, where the equations of PBCs are shown in Supplementary Note 1 (**SN1**). The displacement gradient defining the strain state of the RVE is $\boldsymbol{H}$. Examples of the imposed displacement gradients of uniaxial compression in 3 direction and pure shear in 6 direction were given by Eq. (5) and (6) (**Fig. 2b**):

$$\boldsymbol{H} = \begin{bmatrix} 0 & 0 & 0 \\ 0 & 0 & 0 \\ 0 & 0 & \varepsilon \end{bmatrix} \quad (5),$$

$$\boldsymbol{H} = \begin{bmatrix} 0 & \gamma & 0 \\ \gamma & 0 & 0 \\ 0 & 0 & 0 \end{bmatrix} \quad (6),$$

where ε and γ denote the uniaxial and shear strain, respectively. Stress contours of two representative simulations on the DS-dTPMS with 50% relative density using PBCs were given in **Fig. S1e,f**.

After simulations, the volume-averaged stresses due to the applied deformation were calculated using the following equation:

$$\bar{\sigma} = \frac{\sum_{n=1}^{N} \int \sigma_{ij}^{n} dV^{n}}{V_{tot}} \quad (7),$$

, where $\bar{\sigma}$ is the volume-averaged stress, σ_{ij}^{n} is the stress in ij direction (i.e., 1 to 6 directions as defined above) of the n-th element, V^{n} is the volume of n-th element, N is the total number of elements.

3D transformation of stiffness matrix: After obtaining the stiffness matrices for diamond-TPMS microlattices, the matrices were transformed to calculate the elastic property values, i.e., elastic modulus ($E_{[hkl]}$), shear modulus ($G_{[hkl]}^{12}$), and Poisson's ratio ($v_{[hkl]}^{12}$), in any arbitrary directions $[hkl]$ in 3D (**Fig. 2b**). Here $[hkl]$ represents the direction in an orthogonal coordinate system in which 1, 2, and 3 directions defined above are considered as $[100]$, $[010]$, and $[001]$ directions, respectively. To calculate the properties, the stiffness matrix obtained from simulations was transformed to the direction $[hkl]$ using:

$$C' = NCN^{T} \quad (8),$$

where N^{T} is the transpose of the transformation matrix N as shown in **SN2**, C and C' are the original and transformed stiffness matrices, respectively. The elastic property can then be calculated by using the following relationships (see detailed derivations in **SN2**):

$$\begin{cases} E_{[hkl]} = \dfrac{1}{S'_{11}} \\ \bar{G}_{[hkl]}^{12} = \dfrac{1}{2\pi} \displaystyle\int_{0}^{2\pi} G_{[hkl],\theta}^{12} d\theta \\ \bar{v}_{[hkl]}^{12} = \dfrac{1}{2\pi} \displaystyle\int_{0}^{2\pi} v_{[hkl],\theta}^{12} d\theta \end{cases} \quad (9),$$

where $\bar{G}_{[hkl]}^{12}$ and $\bar{v}_{[hkl]}^{12}$ are averaged shear modulus and averaged Poisson's ratio values, respectively, obtained from the transformed 2-3 plane (the $y'' - z''$ plane as shown in **Fig. S2)**, $S' = (C')^{-1}$ is the transformed compliance matrix, θ is the rotational angle on $y'' - z''$ plane (**Fig. S2**). Similarly, the elastic

property values of solid single-crystalline calcite can be also calculated. These directional values of elastic properties can be visualized as 3D contours (**Fig. 2b**).

3. Results

3.1. Dual-scale diamond-TMPS microlattice in ossicles

The skeletal system of the starfish *P. nodosus* consists of an assembly of calcite-based, millimeter-sized ossicles (**Fig. 1a**). The ossicles have a periodic lattice-like stereom structure which has been previously determined to be a diamond-TPMS microlattice with a relative density of ca. 50 vol% (**Fig. 1b-d**) [33]. **Fig. 1c,d** show a representative volume isolated from an ossicle and the corresponding 3D-FFT result, demonstrating the diamond-TPMS microlattice structure of "$Fd\bar{3}m$" symmetry (unit cell size of 34.6 ± 8.0 μm and branch length of 15.0 ± 3.4 μm). An RVE of diamond-TPMS microlattice with 50% relative density as shown in **Fig. 1e** can be used as an idealized model to represent the microlattice structure of ossicles. We also observed that the [111] direction of the diamond-TPMS microlattice in ossicles is usually aligned with the normal direction of the starfish, which is defined as the direction perpendicular to the plane formed by the five arms of the starfish (**Fig. 1b**) [33].

In addition to the lattice-level single-crystallinity, each ossicle is made of single-crystalline calcite at atomic-level [33]. This is evident from the epitaxial overgrowth experiment, where the overgrown calcite crystals all follow the same orientation as the underlying ossicle (**Fig. 1f**). Please see details of overgrowth experiments in SN5. This overgrowth experiment also reveals that the [111] direction of the diamond lattice is aligned with the c-axis of calcite as schematically shown in **Fig. 1g**. Furthermore, the three-fold symmetry of the basal plane of calcite is aligned with the three-fold symmetry of the diamond lattice: the non-[111] branches in the diamond lattice generally follow the direction of the intersected edges of two adjacent $\{10\bar{1}4\}$ cleavage planes of calcite, i.e., the $\langle 4\bar{4}0\bar{1}\rangle$ directions [33] (**Fig. 1g** and **Fig. S3**). This results in the so-called dual-scale single-crystalline microlattice.

3.2. 3D elastic properties

To evaluate the mechanical properties of the dual-scale microlattice in starfish ossicles, we built four models for mechanical modeling comparison as introduced in methods: (1) the solid calcite, (2) I-dTPMS: a diamond-TPMS microlattice with equivalent isotropic calcite properties, (3) DS-dTPMS: a dual-scale diamond-TPMS microlattice as observed in ossicles, and (4) DS-dTPMS (180°): a modified DS-dTPMS microlattice with calcite rotated by 180° about its c-axis (**Fig. 2a**). The 3D elastic properties of these four models were then calculated using the four-step workflow described in Methods, including (1) the FE simulation configurations of material properties, PBCs, and mechanical loading, (2) calculation of the full stiffness matrices of all four models, (3) 3D transformation of the obtained stiffness matrices, and (4) visualization of the 3D elastic property contours (**Fig. 2b**).

We first conducted detailed analysis of the mechanical properties of the DS-dTPMS in starfish ossicles in comparison to solid calcite and I-dTPMS microlattice. Representative 3D contours of elastic modulus ($E_{[hkl]}$), averaged shear modulus ($\bar{G}^{12}_{[hkl]}$), and averaged Poisson's ratio ($\bar{v}^{12}_{[hkl]}$) of the solid calcite, I-dTPMS microlattice, and DS-dTPMS microlattice at 50% relative density, were shown in **Fig. 3**. The maximum, and minimum shear modulus and Poisson's ratio contours (i.e., G_{max}, v_{max}, G_{min}, and v_{min}), respectively, as well as 2D visualizations of all elastic properties of all models were summarized in **SN3** and **Fig. S4-9**.

For solid calcite, the elastic modulus contour exhibits a three-fold symmetry about its c-axis, resembling a 6-pointed star-like shape, agrees with the previous result (**Fig. 3a,b, Table S1**) [37]. For some characteristic planes of calcite, such as $(10\bar{1}4)$, $(10\bar{1}8)$, and (0001), the moduli are calculated as 72.4

GPa, 74.8 GPa and 74.6 GPa along their plane normals, respectively, which agree well with the previous values obtained from simulations and indentation experiments and hence validate our calculation process (**Table S3**) [33,38,39]. We also found that the maximum elastic moduli of 152.9 GPa are along $\langle 5\bar{5}01\rangle$ directions. The directions close to the c-axis are generally more compliant, and the minimum elastic moduli of 72.0 GPa are along $\langle 10\bar{1}\frac{23}{50}\rangle$ directions (**Fig. 3b**). Moreover, the 3D contours of $\bar{G}^{12}_{[hkl]}$ and $\bar{\nu}^{12}_{[hkl]}$ of calcite also show the trigonal symmetry where the directions with high $E_{[hkl]}$ has relatively low $\bar{G}^{12}_{[hkl]}$ and $\bar{\nu}^{12}_{[hkl]}$ (**Fig. 3b-d**).

For I-dTPMS microlattice, the elastic modulus contour exhibits a three-fold symmetry about the $[111]$ direction due to the trigonal symmetry of the diamond-TPMS lattice and possesses a cube-like shape (**Fig. 3e,f, Table S2**) [40]. Furthermore, the calculated elastic moduli of $[1\bar{1}0]$, $[111]$, and $[100]$ directions are 27.2 GPa, 30.9 GPa, and 20.1 GPa, which match with the previously reported values and, thus again, validate our simulation and calculation process [33,35]. Again, we found that the maximum elastic moduli of 30.9 GPa are along $\langle 111\rangle$ directions, while the minimum elastic moduli of 20.1 GPa are along $\langle 100\rangle$ directions (**Fig. 3f**). Similarly, **Fig. 3g,h** show the 3D contours of $\bar{G}^{12}_{[hkl]}$ and $\bar{\nu}^{12}_{[hkl]}$ of I-dTPMS, further demonstrating that the directions with high $E_{[hkl]}$ has relatively low $\bar{G}^{12}_{[hkl]}$ and $\bar{\nu}^{12}_{[hkl]}$ (**Fig. 3g-h**).

For DS-dTMPS microlattice, its elastic modulus contour merges the morphological characteristics of the elastic modulus contours of calcite and I-dTPMS together, resulting in a "Saturn"-like geometry with trigonal symmetry (**Fig. 3i,j, Table S2**). In this case, the stiff $[111]$ direction of the diamond-TPMS microlattice is coaligned with the compliant c-axis of calcite (**Fig. 3i,j**) [33]. In addition, the directions of minimum elastic modulus ($[0\bar{1}1\frac{23}{50}]$, $[\bar{1}10\frac{23}{50}]$, and $[10\bar{1}\frac{23}{50}]$ directions, respectively, cyan arrows in **Fig. 3b**) in calcite are approximately aligned (22.6° difference relative to c-axis) with the directions of the highest elastic modulus in I-dTPMS microlattice ($[1\bar{1}\bar{1}]$, $[\bar{1}1\bar{1}]$ and $[\bar{1}\bar{1}1]$ directions, red arrows in **Fig. 3f**). Therefore, the dual-scale coalignment in DS-dTPMS allows the elastic modulus compensation in 3D and results in a nearly transversely isotropic shape of its elastic modulus contour (**Fig. 3j**). This morphological combination can also be observed in the $\bar{G}^{12}_{[hkl]}$ and $\bar{\nu}^{12}_{[hkl]}$ contours (**Fig. 3k,l**). We performed FE simulations to validate the theoretically calculated elastic modulus values at several orientations of the DS-dTPMS, which demonstrates the accuracy of our prediction method (**SN4**, **Fig. S10**, and **Table S4**).

3.3. Effect of relative density

We next explore how the relative density affects the structural-mechanical properties of the dual-scale microlattice, and whether the often-observed 50% relative density in ossicles possesses any special structural-mechanical significances.

For I-dTPMS, as the relative density increases, the faces of the cube-like shape of the elastic modulus contour become less concave, agreeing with previous results [40] (**Fig. 4a**). This leads to an increase in overall mechanical isotropy. For DS-dTPMS, the elastic modulus contour first becomes smoother and more isotropic up to 60% relative density, however, it starts to resemble the morphology of elastic modulus contour of calcite beyond 70% relative density (**Fig. 4b** and **Table S2**). This is expected since the increase of relative density of the microlattice results in the increased similarity of mechanical properties to its bulk constituent. The change in mechanical isotropy as a function of relative density can be more quantitatively represented by a universal anisotropic index calculated based on the full stiffness matrix (**Fig. 4c**) [41]. The higher the index, the lower the mechanical isotropy. The results reveal that the anisotropic indices of DS-dTPMS are always higher than those of the I-dTPMS, where their values are always smaller than that of calcite. The anisotropic indices closely approach to each other as the relative density reaches 60% (**Fig. 4c**). Furthermore, for DS-dTPMS, the anisotropic indices of 60% and 70% relative densities are similar,

implying a minimal value in between as proposed above (**Fig. 4b,c**). Therefore, the dual-scale coalignment in ossicles improves the mechanical isotropy significantly compared to calcite, however, 50% is not the relative density that maximizes the isotropy.

Other than the 3D distributions, the elastic modulus values also depend on relative densities (**Fig. 4d**). As expected, the higher the relative densities, the larger the elastic modulus in general (**Fig. 4d**). In addition, all distributions show two peaks where one is at the lower end while another is at the higher end. Among them, the DS-dTPMS with 50% relative density has elastic moduli ranging from 17 to 30 GPa with peaks at ca. 19 and 29 GPa.

Other than mechanical properties, we also investigated the effect of relative density on the structural characteristics of diamond-TPMS microlattice (**Fig. 4e-g**). First of all, the diamond-TPMS microlattice with 50% relative density yields the zero mean surface curvature ($H = 0$), while others result in the constant-mean-curvature surfaces (**Fig. 4e, Fig. S11,** and **Table S5**) [42]. The increase of relative density changes H from positive to negative values, suggesting that the surfaces become less curved (**Fig. 4e**). Secondly, we found that SAV of the diamond-TPMS microlattice with relative density of 50% is maximal, regardless of the change of unit cell size (**Fig. 4f, Table S5,6**) [43]. Thirdly, we calculated the throat size (r_{throat}), which is defined as the smallest radius in the void phase, and the minimal solid branch thickness (r_{min}) of the diamond-TPMS microlattice (**Fig. 4g**). As expected, the increase of relative density yields lower r_{throat} and higher r_{min}, while at 50% relative density, $r_{throat} \approx r_{min}$. We previously have shown that the small throat size in natural ceramic foams such as sea urchin spines provides an efficient mechanism to locally jam the fractured fragments during deformation, leading to enhanced energy absorption capability [33,44]. Therefore, with the throat size comparable to the minimal branch size at 50% relative density, the structure may contribute to efficient jamming for improved toughening behavior as observed in [33].

3.4. Effect of dual-scale coalignment

We next investigated the effects of the crystallographic coalignment configurations on the mechanical properties. In starfish ossicles, the match of the two three-fold symmetries of calcite and diamond is achieved via a specific coalignment, i.e., $[0001]_{\text{calcite}}//[111]_{\text{diamond}}$ and $[4\bar{4}0\bar{1}]_{\text{calcite}}//[11\bar{1}]_{\text{diamond}}$. If we rotate calcite by 180° about c-axis while keeping the diamond-TPMS lattice unchanged, we will obtain a new dual-scale microlattice, i.e., DS-dTPMS (180°) (**Fig. 2, Fig. S12**). In this DS-dTPMS (180°), both three-fold symmetries of calcite and diamond lattice are also precisely registered. However, in stark contrast to the increased mechanical isotropy due to 3D property compensation observed in DS-dTPMS, the DS-dTPMS (180°) microlattice has decreased mechanical isotropy (**Fig. 5b, Fig. S13-17, and Table S7**). This is because, for DS-dTPMS (180°), the misorientation angle between the stiffest directions of calcite ($[5\bar{5}01]$, $[05\bar{5}1]$, and $[\bar{5}051]$) and the stiffest directions of the diamond lattice ($[\bar{1}11]$, $[1\bar{1}1]$and $[11\bar{1}]$) is only 2.5° relative to c-axis. The increase in mechanical anisotropy for DS-dTPMS (180°) can be demonstrated by the 3D elastic modulus contour of DS-dTPMS (180°) which maintains 6-pointed star-like shape similar to that of calcite (**Fig. 5b**). Moreover, the isotropy improvement and reduction for DS-dTPMS and DS-dTPMS (180°), respectively, can be also visualized in the shear moduli distribution on a representative plane (**Fig. 5c,d**). Specifically, for DS-dTPMS, the highest shear modulus of calcite is approximately aligned with the lowest shear modulus of I-dTPMS, exhibiting the property compensation for improved mechanical isotropy (**Fig. 5c**). While for DS-dTPMS (180°), the closely aligned directions with highest shear moduli of both calcite and I-dTPMS increase and decrease the maximum and minimum shear moduli, respectively, compared to I-dTPMS, enhancing the mechanical anisotropy (**Fig. 5d**). We further calculated the universal anisotropic indices for the microlattices, which confirmed that the mechanical anisotropy of DS-dTPMS (180°) is higher than DS-dTPMS at relative density over 40% and nearly independent of the change of relative density (**Fig. 5e**).

So far, our analyses are primarily focused on elastic properties. Fracture behavior, particularly for those constituents that undergo cleavage fracture, is an important aspect to consider. Here, to demonstrate the effects of cleavage fracture behavior on the strength of dual-scale single-crystalline lattices, we considered a bio-inspired dual-scale diamond lattice made of single-crystalline geological calcite (**Fig. 5f**). Geological calcite is known to undergo easy fracture along cleavage planes, i.e., $(10\bar{1}4)$, $(\bar{1}104)$, and $(0\bar{1}14)$, while cleavage fracture is suppressed in biogenic calcite in stereoms due to the nanoscopic intra-crystalline organic inclusions [45,46]. To simplify, the shear effect of the branches is neglected, which requires the bioinspired dual-scale lattice to have low density or large branch length-to-thickness ratio. We considered a compressive loading along the $[111]$ direction of the diamond lattice, which induces bending stress on the inclined (i.e., non-$[111]$) branches (denoted as $\sigma_{bending}^{non-[111]}$) (**Fig. 5f**). The corresponding resolved normal stress on the cleavage planes of the calcite-based branches, denoted as $\sigma_{tension}^{cleavage}$, can then be calculated as $\sigma_{tension}^{cleavage} = \sigma_{bending}^{non-[111]} \cdot (cos\,^2\alpha)$. Here, α is defined as the angle between the bending stress and the normal direction of the cleavage planes of calcite, and $cos\,^2\alpha$ is defined as the resolved stress factor (SF) (**Fig. 5f**) [47]. Next, we introduce a dual-scale misorientation angle γ, which is the azimuthal angle between the original 1-axis and rotated 1'-axis with respect to c-axis of calcite (**Fig. 5f**). Therefore, $\gamma = 0°$ corresponds to the coalignment in DS-dTPMS microlattice, while $\gamma = 180°$ corresponds to that of the DS-dTPMS (180°) microlattice (**Fig. 2a**). At a given γ, we can use SF as the measure of the resolved normal stress on different cleavage planes, and determine the maximum scenario of SF (or SF_{max}) (**Fig. 5g**). The increase of SF_{max} results in increased maximum of $\sigma_{tension}^{cleavage}$ among cleavage planes, indicating the decreased strength of the dual-scale diamond lattice with given γ. Considering the three equivalent cleavage planes of calcite across all γ values, we found that, at $\gamma = 0°$, the bioinspired diamond lattice has highest $SF_{max} = 0.81$, while when $\gamma = 180°$, it has the smallest $SF_{max} = 0.32$ (**Fig. 5g**). Therefore, although $\gamma = 0°$ results in the highest isotropy of elastic properties due to property compensation, it yields the lowest strength among all surveyed γ based on the simplified analyses (**Fig. 5g**).

4. Discussions

The calcitic ossicles in the starfish *P. nodosus* possess a unique dual-scale single-crystalline nature. At atomic scale, it is a single-crystalline calcite, whereas at microlattice level, it is a diamond-TPMS lattice with a relative density of ~50%. In addition, we showed that the crystallographic symmetries at these two length scales are precisely registered following $[0001]_{\text{calcite}}//[111]_{\text{diamond}}$ and $[4\bar{4}0\bar{1}]_{\text{calcite}}//[1\bar{1}\bar{1}]_{\text{diamond}}$. The combined computational and theoretical methodology developed here allows us to investigate the mechanical properties of this unique DS-dTPMS microlattice. Our results suggest that, in 3D, the DS-dTPMS microlattice achieves enhanced mechanical isotropy by aligning the compliant and stiff directions from calcite and diamond-TPMS lattice together. This enhanced mechanical isotropy in ossicles, particularly within the basal plane, i.e., the (0001) plane in calcite or (111) plane in diamond lattice, may be beneficial for the biomechanical performance of starfish. In the starfish endoskeletal system, the ossicles are arranged as a tessellated array, where the adjacent ossicles are connected by fibrous tissue [48]. During locomotion, the ossicles resist in-plane compressive and tensile loads resulted from the relative movements of ossicles and fibers in various directions, particularly within the basal plane [48,49]. The enhanced mechanical isotropy may reduce deformation mismatch among adjacent ossicles. Further analysis of the mechanical performance of the ossicles assembly are needed to provide more insights in this regard [49,50]. Moreover, the above computations and analysis were allowed by the fact that the ossicles are constructed by a single-crystalline calcite. For stereom exhibiting different crystallographic orientations of the constituent calcite or the lattice structure at different domains, such mechanical compensation due to symmetry matching need to be reanalyzed, as such coalignment may be lost.

We also note that despite the increase of mechanical isotropy for DS-dTPMS in ossicles due to 3D property compensation, the mechanical isotropy is not maximized at 50% relative density as observed in

ossicles. Instead, the maximized isotropy is achieved when the relative density is within 60%-70%, beyond which the 3D modulus contour of DS-dTPMS approaches to that of calcite. Therefore, if maximizing mechanical isotropy is one of the driving forces of evolutionary selection for ossicles' microstructure, other driving factors should also play roles in determining the microscopic structural characteristics of ossicles. For example, we show that 50% relative density in diamond-TPMS yields the zero mean surface curvature and highest SAV ratio. This minimal surface structure can avoid stress concentration to improve strength and damage tolerance compared to sharp connections between branches [51,52]. In addition, it has been previously postulated that the minimal surface and highest SAV in echinoderm stereom provide maximum contact between the stroma within the void phase and mineralized phase, which may maximize the biomineralization efficiency [53]. Another factor may be related to the damage tolerance of stereom by considering the jamming mechanism of fractured fragments. By having similar r_{throat} and r_{min} values in the diamond-TPMS microlattice at 50% relative density, the fractured fragments from the solid branches can be efficiently jammed locally by the small throat openings, leading to the formation of densified damage bands and contributing enhanced energy dissipation [33,44]. Therefore, the observed 50% relative density may be a compromised result considering mechanical properties (isotropy, stress distribution, damage tolerance via local jamming), light weight, and formation pathways.

Regarding the particular dual-scale coalignment observed in ossicles (i.e., $[0001]_{\text{calcite}}//[111]_{\text{diamond}}$ and $[4\bar{4}0\bar{1}]_{\text{calcite}}//[1\bar{1}\bar{1}]_{\text{diamond}}$), our results indicate that other alignments, particularly DS-dTPMS (180°) which is achieved by rotating the calcite about its c-axis by 180°, exhibits reduced mechanical isotropy. Note here that the DS-dTPMS (180°) microlattice still maintains a precise registration of two three-fold symmetries from atomic and microscopic scales. However, it is not appropriate to conclude that the particular crystallographic coalignment in ossicles is a result of maximizing mechanical isotropy. Other factors like particular growth or the biomineralization process may play a significant role here. On one hand, it is known that the growth of sea urchin larval spicules and some calcareous sponges grow their spicules along specific crystallographic directions, namely, along their a^* axes [54–56], which is different from the DS-dTPMS microlattice here. On the other hand a diverse variety of stereom microstructures in echinoderm skeletal elements exists, which range from fully stochastic porous structure [27] to the highly regular microlattice as seen in the starfish ossicles here. Most of these structures all diffract as single crystals [23]. In these cases, the branches in stereom microscopically do not necessarily have to align with any specific crystallographic orientations of constituent calcite. This suggests that it is theoretically possible that echinoderms can produce the diamond microlattice with a different calcite orientation. Therefore, it is still an open question why this particular coalignment is achieved in the starfish ossicles.

Furthermore, other than the mechanical isotropy, strength is another critical factor in designing dual-scale lattices. Here, we proposed a dual-scale geometrical analysis method to study the effect of cleavage fracture behavior on strength of dual-scale lattices. By varying the dual-scale misorientation angle (γ), we found that the external loading that induces cleavage fracture can be increased at $\gamma = 180°$ which improves the strength of dual-scale lattices. This method can be extended to predict the fracture behavior of other dual-scale lattices with constituent experiencing easy cleavage fracture.

5. Conclusions

In this work, we investigated the mechanical properties of the dual-scale (i.e., atomic-scale and lattice-scale) crystallographic coalignment found in the ossicles of *P. nodosus*. We first utilized a combined theoretical and computational method to predict the structural symmetry and 3D elastic property contours of dual-scale diamond-TPMS microlattice in ossicles. The results demonstrate that the ossicles with 50% relative density are a structural feature of improved yet unmaximized mechanical isotropy among surveyed relative densities and dual-scale coalignments. Combining the structural analysis, we propose that the ossicles possess a trade-off between mechanical (i.e., mechanical isotropy, improved stiffness, strength, and toughness) and morphological advantages (i.e., zero mean curvature and highest surface-to-volume

ratio). Finally, we envision that the method in this work can be adopted to understand other echinoderm stereoms made of single-crystalline calcite and design dual-scale microlattice for desired mechanical isotropy, strength and structural symmetry.

Acknowledgements. We gratefully acknowledge the Air Force Office of Scientific Research under award number FA9550-19-1-0033 and the National Science Foundation (DMR-1942865) for supporting this work. We also thank Dr. Ting Yang from the Massachusetts Institute of Technology for providing the experimental result of crystal overgrowth. We thank Dr. P. D. Shevchenko and Dr. F. De Carlo for help with collecting the synchrotron-based μ-CT data at the Advanced Photon Source (APS) in the Argonne National Lab, and Dr. S. McCartney and Dr. Y.-P. Yu at the Nanoscale Characterization and Fabrication Laboratory (NCFL) at the Virginia Tech for assistance in scanning electron microscopy. This research used resources of the Advanced Photon Source, a U.S. Department of Energy (DOE) Office of Science User Facility operated for the DOE Office of Science by Argonne National Laboratory under Contract No. DE-AC02-06CH11357.

Author contributions: L.L. supervised the research and conceived the idea; L.L. and H.C. designed the research; H.C. and Z.J. performed the research; H.C., and Z.J., Z.D., and L.L. analyzed data; H.C., Z.J., Z.D., and L.L. wrote the paper.

The authors declare no conflict of interest.

Figures

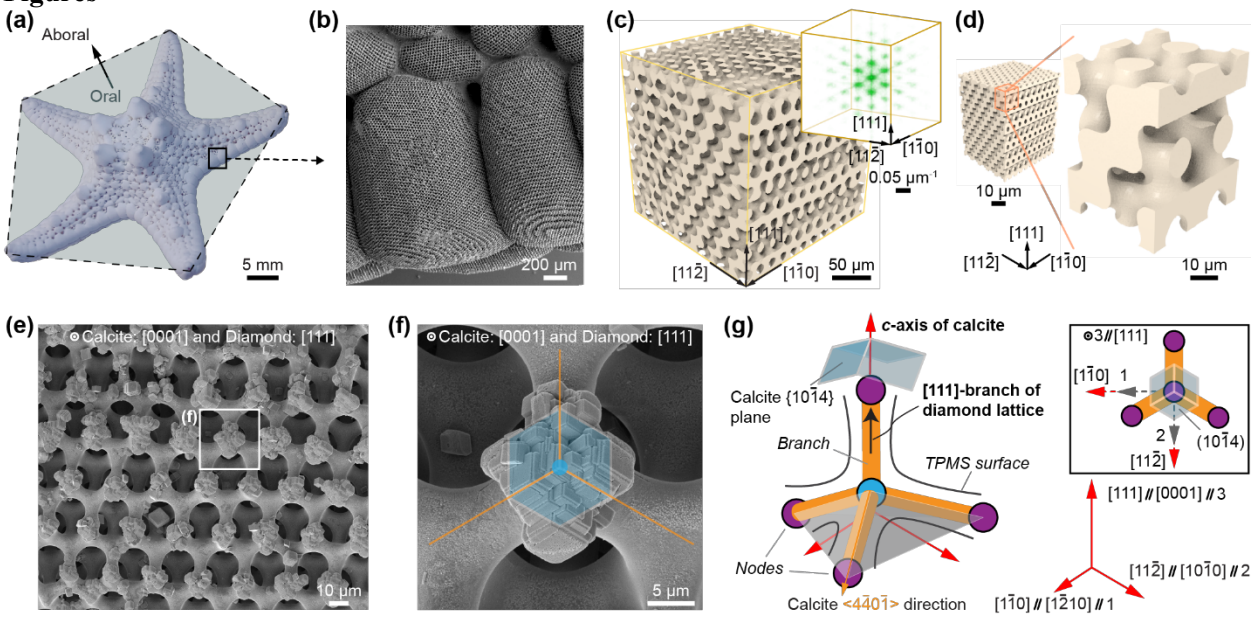

Figure 1. Dual-scale crystallographic coalignment in the ossicles of starfish *Protoreaster nodosus*. (**a**) The endoskeleton of starfish *P. nodosus*, showing radially-arranged arrays of ossicles and the normal direction (black solid arrow) from the oral to aboral sides. The cyan plane roughly indicates the plane of the starfish perpendicular to the normal direction. (**b**) SEM image of the ossicles where the exposed crystallographic planes of (111) are closely parallel to the plane of starfish. (**c**) A cubic volume of stereom in the ossicle. Here, the [111] direction is along the normal direction of the starfish's skeleton. Inset: 3D-FFT pattern of the cubic volume of an ossicle with diffraction spots. (**d**) The RVE of diamond-TPMS microlattice as a model to represent the lattice-scale structure of ossicles. (**e**) Scanning electronic microscope (SEM) image of the calcite crystals overgrown on the underlying ossicle. (**f**) Zoom-in image of the crystallographic orientation coalignment between the intersection between two adjacent {10$\bar{1}$4} cleavage planes (cyan planes) of calcite and the inclined branches (orange lines) of ossicle's diamond-TPMS microlattice. (**g**) Schematic of the dual-scale coalignment between atomic-scale crystallography of calcite and lattice-scale crystallography of diamond-TPMS microlattice in ossicles.

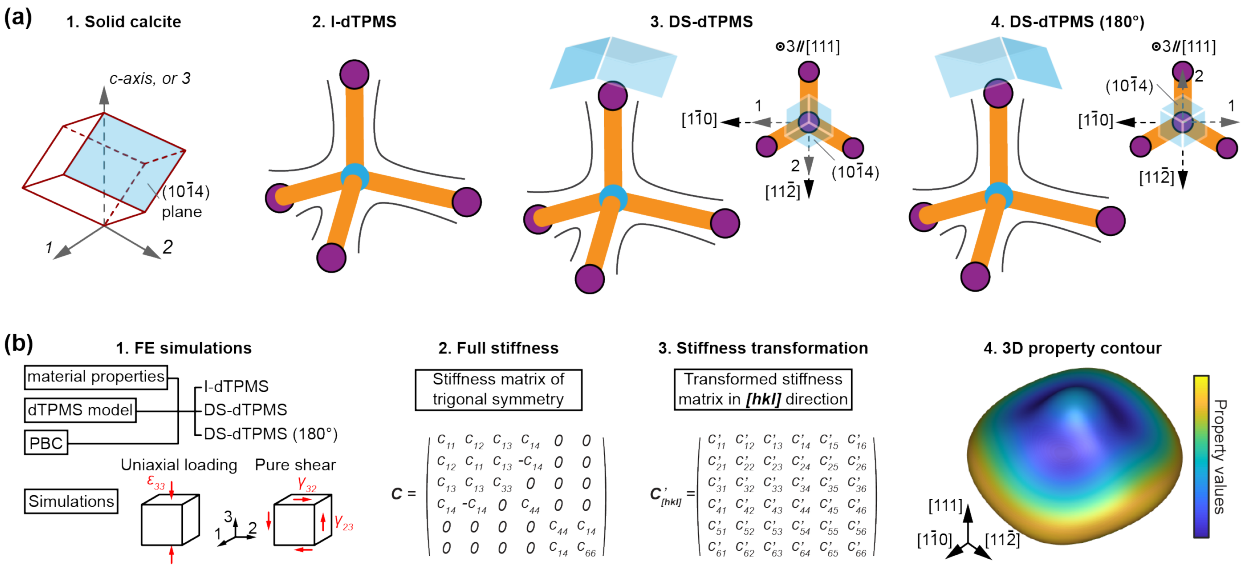

Figure 2. Introduction to models and methodology. (**a**) Schematic models of (1) single-crystalline solid calcite, (2) I-dTPMS, (3) DS-dTPMS, and (4) DS-dTPMS (180°). Here, DS-dTPMS represent an idealized model of ossicles. (**b**) Methodology of the elastic properties prediction, including (1) material properties and PBC configurations for FE simulations, (2) calculation of the full stiffness matrix of four models, (3) transformation of the full stiffness matrix to calculate elastic properties in any arbitrary $[hkl]$ directions, and (4) visualization of the 3D elastic property contour.

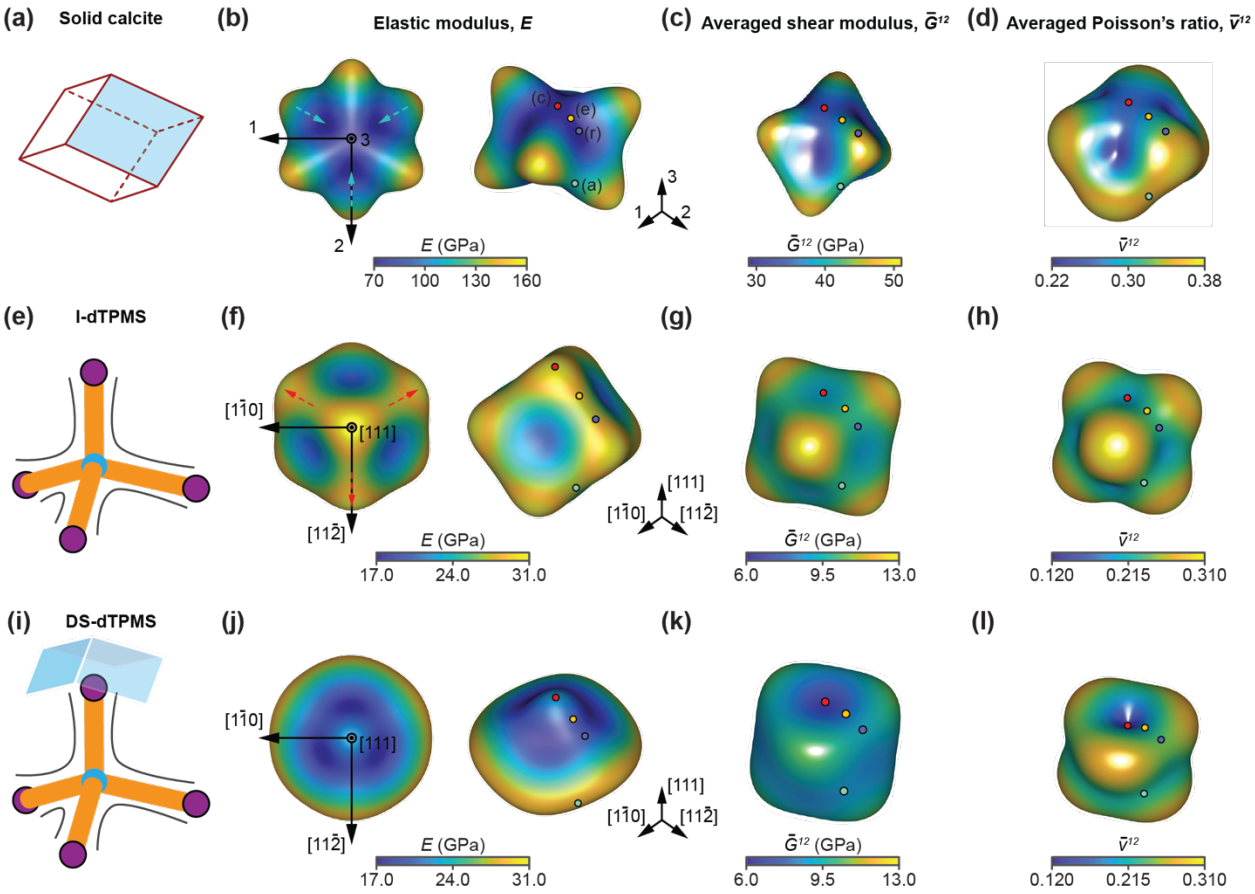

Figure 3. 3D elastic property contours of single-crystalline calcite, I-dTPMS, and DS-dTPMS. (**a**) Geometrical representation of the calcite's crystallographic symmetry. (**b-d**) 3D contours of elastic modulus $E_{[hkl]}$ (**b**), averaged shear modulus $\bar{G}^{12}_{[hkl]}$ (**c**), and averaged Poisson's ratio $\bar{\nu}^{12}_{[hkl]}$ (**d**) of calcite, respectively. The top view (-3 direction) of the 3D elastic modulus contour of calcite is shown, in which the cyan arrows indicate the most compliant directions of calcite. (**e**) Geometrical representation of crystallographic symmetry of I-dTPMS. (**f-h**) 3D contours of elastic modulus $E_{[hkl]}$ (**f**), averaged shear modulus $\bar{G}^{12}_{[hkl]}$ (**g**), and averaged Poisson's ratio $\bar{\nu}^{12}_{[hkl]}$ (**h**) of I-dTPMS, respectively. The $[\bar{1}\bar{1}\bar{1}]$ view of the 3D elastic modulus contour of I-dTPMS is shown, in which the red arrows indicate the stiffest directions of I-dTPMS. (**i**) Geometrical representation of the resultant crystallographic symmetry of DS-dTPMS. (**j-l**) 3D contours of elastic modulus $E_{[hkl]}$ (**j**), averaged shear modulus $\bar{G}^{12}_{[hkl]}$ (**k**), and averaged Poisson's ratio $\bar{\nu}^{12}_{[hkl]}$ (**l**) of DS-dTPMS, respectively. The view along $[\bar{1}\bar{1}\bar{1}]$ direction of the 3D elastic modulus contour of DS-dTPMS is shown. Here, the red (c), yellow (e), blue (r), and green (a) dots on all 3D elastic property contours indicate the property values of the c-axis direction, plane normal of $(10\bar{1}8)$, plane normal of $(10\bar{1}4)$, and $[2\bar{1}\bar{1}0]$ direction (a_1-axis). Their values are summarized in **Table S3**.

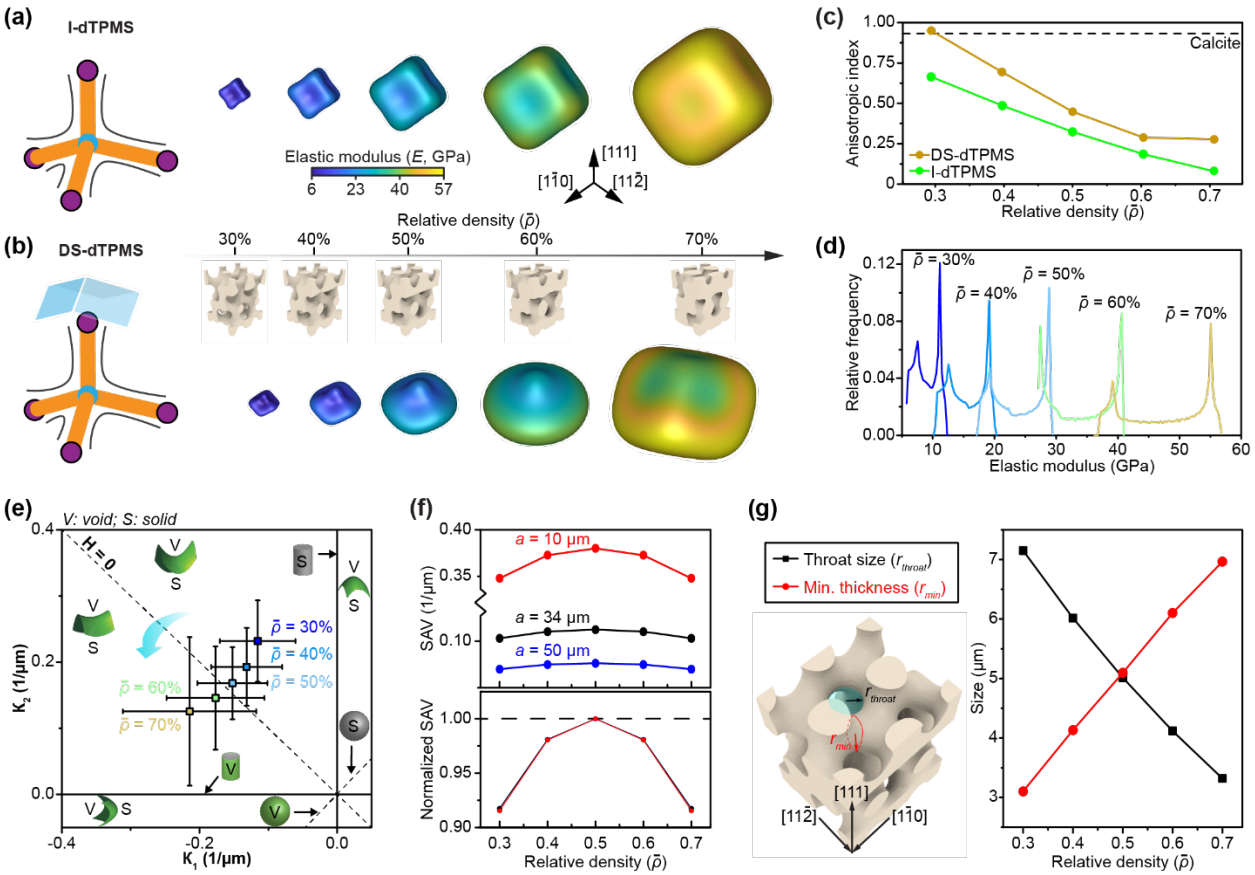

Figure 4. Effect of relative density on the mechanics and structure of DS-dTPMS. (**a**,**b**) Evolution of the 3D elastic modulus contours of the I-dTPMS (**a**) and DS-dTPMS (**b**) with various relative densities. (**c**) Universal anisotropic index of I-dTPMS, and DS-dTPMS with different relative densities, respectively. (**d**) Histogram representation of distributions of elastic modulus of DS-dTPMS with different relative densities. (**e**) Mean surface curvatures of the diamond-TPMS microlattice with 34 μm unit cell size and different relative densities. The standard deviations of principal curvatures κ_1 and κ_2 are used for error bars. (**f**) SAV (surface-area-to-volume ratio) and normalized SAV by the maximum value of various relative densities and unit cell sizes. (**g**) Throat size (r_{throat}) and minimal branch thickness (r_{min}) of diamond-TPMS microlattice with 34 μm unit cell size and different relative densities.

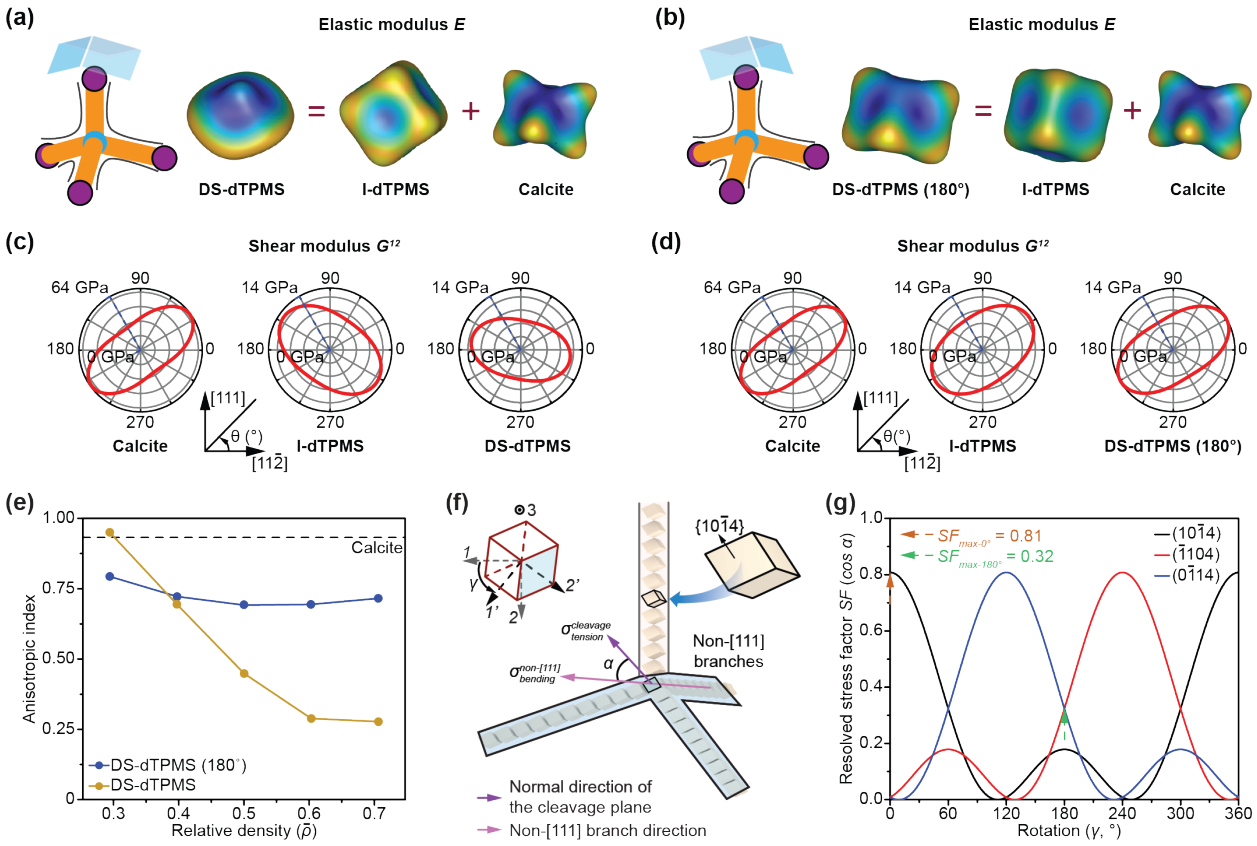

Figure 5. Effect of dual-scale coalignment. (**a**) Schematic representation of the property compensation of DS-dTPMS. (**b**) Schematic representation of the anisotropy enhancement of DS-dTPMS (180°). (**c,d**) Shear moduli on the $(1\bar{1}0)$ plane of DS-dTPMS (**c**) and DS-dTPMS (180°) (**d**), respectively. (**e**) Universal anisotropic index of DS-dTPMS and DS-dTPMS (180°) with different relative densities, respectively. (**f**) Schematic of the dual-scale crystallographic coalignment in a dual-scale diamond lattice. Blue area: three inclined or non-[111] branches; γ: misorientation angle of the single-crystalline calcite about its c-axis from 1-direction; α: angle between the normal direction of the cleavage plane (purple arrow) and the longitudinal direction of the non-[111] branch (pink arrow); $\sigma_{bending}^{non-[111]}$ denotes the bending stress on the non-[111] branch, while $\sigma_{tension}^{cleavage}$ denotes the normal resolved stress on the cleavage plane; cyan box: $(10\bar{1}4)$ plane. (**g**) Relationship between γ and resolved stress factor SF $((\cos\alpha)^2)$. Orange arrow indicates $SF_{max-0^\circ} = 0.81$ which is the maximum SF_{max} for $\gamma = 0°$. Green arrow indicates $SF_{max-180^\circ} = 0.32$ which is the maximum SF_{max} for $\gamma = 180°$.

References:

[1] X. Zheng, H. Lee, T.H. Weisgraber, M. Shusteff, J. DeOtte, E.B. Duoss, J.D. Kuntz, M.M. Biener, Q. Ge, J.A. Jackson, S.O. Kucheyev, N.X. Fang, C.M. Spadaccini, Ultralight, ultrastiff mechanical metamaterials, Science. 344 (2014) 1373–1377. https://doi.org/10.1126/science.1252291.

[2] L.R. Meza, S. Das, J.R. Greer, Strong, lightweight, and recoverable three-dimensional ceramic nanolattices, Science. 345 (2014) 1322–1326. https://doi.org/10.1126/science.1255908.

[3] T.A. Schaedler, W.B. Carter, Architected Cellular Materials, Annu. Rev. Mater. Res. 46 (2016) 187–210. https://doi.org/10.1146/annurev-matsci-070115-031624.

[4] V.S.S. Deshpande, M.F.F. Ashby, N.A.A. Fleck, Foam topology: bending versus stretching dominated architectures, Acta Mater. 49 (2001) 1035–1040. https://doi.org/Doi 10.1016/S1359-6454(00)00379-7.

[5] J. Bauer, A. Schroer, R. Schwaiger, O. Kraft, Approaching theoretical strength in glassy carbon nanolattices, Nat. Mater. 15 (2016) 438–443. https://doi.org/10.1038/nmat4561.

[6] J.B. Berger, H.N.G. Wadley, R.M. McMeeking, Mechanical metamaterials at the theoretical limit of isotropic elastic stiffness, Nature. 543 (2017) 533–537. https://doi.org/10.1038/nature21075.

[7] T. Li, X. Hu, Y. Chen, L. Wang, Harnessing out-of-plane deformation to design 3D architected lattice metamaterials with tunable Poisson's ratio, Sci. Rep. 7 (2017) 1–10. https://doi.org/10.1038/s41598-017-09218-w.

[8] A. Zhakatayev, Z. Kappassov, H.A. Varol, Analytical modeling and design of negative stiffness honeycombs, Smart Mater. Struct. 29 (2020). https://doi.org/10.1088/1361-665X/ab773a.

[9] C.S. Ha, R.S. Lakes, M.E. Plesha, Cubic negative stiffness lattice structure for energy absorption: Numerical and experimental studies, Int. J. Solids Struct. 178–179 (2019) 127–135. https://doi.org/10.1016/j.ijsolstr.2019.06.024.

[10] X.Y. Zheng, W. Smith, J. Jackson, B. Moran, H.C. Cui, D. Chen, J.C. Ye, N. Fang, N. Rodriguez, T. Weisgraber, C.M. Spadaccini, Multiscale metallic metamaterials, Nat. Mater. 15 (2016) 1100–1106. https://doi.org/10.1038/nmat4694.

[11] L.R. Meza, A.J. Zelhofer, N. Clarke, A.J. Mateos, D.M. Kochmann, J.R. Greer, Resilient 3D hierarchical architected metamaterials, Proc. Natl. Acad. Sci. U. S. A. 112 (2015) 11502–11507. https://doi.org/10.1073/pnas.1509120112.

[12] L. Zhang, Z. Hu, M.Y. Wang, S. Feih, Hierarchical sheet triply periodic minimal surface

lattices: Design, geometric and mechanical performance, Mater. Des. 209 (2021) 109931. https://doi.org/10.1016/j.matdes.2021.109931.

[13] Y. Chen, Z. Jia, L. Wang, Hierarchical honeycomb lattice metamaterials with improved thermal resistance and mechanical properties, Compos. Struct. 152 (2016) 395–402. https://doi.org/10.1016/j.compstruct.2016.05.048.

[14] R. Xiao, M. Ding, Y. Wang, L. Gao, R. Fan, Y. Lu, Stereolithography (SLA) 3D printing of carbon fiber-graphene oxide (CF-GO) reinforced polymer lattices, Nanotechnology. 32 (2021). https://doi.org/10.1088/1361-6528/abe825.

[15] C. Kenel, N.P.M. Casati, D.C. Dunand, 3D ink-extrusion additive manufacturing of CoCrFeNi high-entropy alloy micro-lattices, Nat. Commun. 10 (2019) 1–8. https://doi.org/10.1038/s41467-019-08763-4.

[16] J. Mueller, J.R. Raney, K. Shea, J.A. Lewis, Architected Lattices with High Stiffness and Toughness via Multicore–Shell 3D Printing, Adv. Mater. 30 (2018) 1–8. https://doi.org/10.1002/adma.201705001.

[17] A. Chortos, J. Mao, J. Mueller, E. Hajiesmaili, J.A. Lewis, D.R. Clarke, Printing Reconfigurable Bundles of Dielectric Elastomer Fibers, Adv. Funct. Mater. 31 (2021) 1–10. https://doi.org/10.1002/adfm.202010643.

[18] H. Cui, R. Hensleigh, D. Yao, D. Maurya, P. Kumar, M.G. Kang, S. Priya, X. (Rayne) Zheng, Three-dimensional printing of piezoelectric materials with designed anisotropy and directional response, Nat. Mater. 18 (2019) 234–241. https://doi.org/10.1038/s41563-018-0268-1.

[19] J.R. Raney, B.G. Compton, J. Mueller, T.J. Ober, K. Shea, J.A. Lewis, Rotational 3D printing of damage-tolerant composites with programmable mechanics, Proc. Natl. Acad. Sci. U. S. A. 115 (2018) 1198–1203. https://doi.org/10.1073/pnas.1715157115.

[20] J.U. Surjadi, L. Gao, K. Cao, R. Fan, Y. Lu, Mechanical Enhancement of Core-Shell Microlattices through High-Entropy Alloy Coating, Sci. Rep. 8 (2018) 1–10. https://doi.org/10.1038/s41598-018-23857-7.

[21] X. Feng, J.U. Surjadi, R. Fan, X. Li, W. Zhou, S. Zhao, Y. Lu, Microalloyed medium-entropy alloy (MEA) composite nanolattices with ultrahigh toughness and cyclability, Mater. Today. 42 (2021) 10–16. https://doi.org/10.1016/j.mattod.2020.10.003.

[22] X. Zhang, J. Yao, B. Liu, J. Yan, L. Lu, Y. Li, H. Gao, X. Li, Three-Dimensional High-Entropy Alloy-Polymer Composite Nanolattices That Overcome the Strength-Recoverability Trade-off, Nano Lett. 18 (2018) 4247–4256. https://doi.org/10.1021/acs.nanolett.8b01241.

[23] G. Donnay, D.L. Pawson, X-ray Diffraction Studies of Echinoderm Plates, Science. 166 (1969) 1147–1150. https://doi.org/10.1126/science.166.3909.1147.

[24] J. Seto, Y.R. Ma, S.A. Davis, F. Meldrum, A. Gourrier, Y.Y. Kim, U. Schilde, M. Sztucki, M. Burghammer, S. Maltsev, C. Jager, H. Colfen, Structure-property relationships of a biological mesocrystal in the adult sea urchin spine, Proc. Natl. Acad. Sci. U. S. A. 109 (2012) 3699–3704. https://doi.org/https://doi.org/10.1073/pnas.1109243109.

[25] K. Okazaki, R.M. Dillaman, K.M. Wilbur, Crystalline axes of the spine and test of the sea urchin Strongylocentrotus purpuratus: Determination by crystal etching and decoration, Biol. Bull. 161 (1981) 402–415. https://doi.org/10.2307/1540945.

[26] D.M. Raup, Crystallography of Echinoid Calcite, J. Geol. 67 (1959) 661–674. https://doi.org/10.1086/626624.

[27] A.B. Smith, Stereom microstructure of the echinoid test, Spec. Pap. Palaeontol. 25 (1980) 1–81.

[28] C.R.C. Paul, A.B. Smith, The early radiation and phylogeny of echinoderms., Biol. Rev. 59 (1984) 443–481. https://doi.org/10.1111/j.1469-185X.1984.tb00411.x.

[29] H. Chen, T. Yang, Z. Wu, Z. Deng, Y. Zhu, L. Li, Quantitative 3D structural analysis of the cellular microstructure of sea urchin spines (II): Large-volume structural analysis, Acta Biomater. 107 (2020) 218–231. https://doi.org/10.1016/j.actbio.2020.03.006.

[30] T. Yang, Z. Wu, H. Chen, Y. Zhu, L. Li, Quantitative 3D structural analysis of the cellular microstructure of sea urchin spines (I): Methodology, Acta Biomater. 107 (2020) 204–217. https://doi.org/10.1016/j.actbio.2020.02.034.

[31] T.B. Grun, J.H. Nebelsick, Structural design of the echinoid's trabecular system, PLoS One. 13 (2018) e0204432. https://doi.org/10.1371/journal.pone.0204432.

[32] T.T. Chen, Microstructure and Micromechanics of the Sea Urchin , Colobocentrotus atratus, (2011).

[33] T. Yang, H. Chen, Z. Jia, Z. Deng, L. Chen, E.M. Peterman, J.C. Weaver, L. Li, A damage-tolerant, dual-scale, single-crystalline microlattice in the knobby starfish, Protoreaster nodosus, Science. 375 (2022) 647–652. https://doi.org/10.1126/science.abj9472.

[34] Z. Jia, H. Chen, Z. Deng, L. Li, Architected microlattices for structural and functional applications: Lessons from nature, Matter. (2023) 1–14. https://doi.org/10.1016/j.matt.2023.01.017.

[35] I. Maskery, A.O. Aremu, L. Parry, R.D. Wildman, C.J. Tuck, I.A. Ashcroft, Effective design and simulation of surface-based lattice structures featuring volume fraction and cell

type grading, Mater. Des. 155 (2018) 220–232. https://doi.org/10.1016/j.matdes.2018.05.058.

[36] Y. Le Page, P. Saxe, J.R. Rodgers, Ab initio stiffness for low quartz and calcite, Phys. Status Solidi Basic Res. 229 (2002) 1155–1161. https://doi.org/10.1002/1521-3951(200202)229:3<1155::AID-PSSB1155>3.0.CO;2-O.

[37] L.-F.F. Zhu, M. Friak, L. Lymperakis, H. Titrian, U. Aydin, A.M.M. Janus, H.-O.O. Fabritius, A. Ziegler, S. Nikolov, P. Hemzalova, D. Raabe, J. Neugebauer, M. Friák, L. Lymperakis, H. Titrian, U. Aydin, A.M.M. Janus, H.-O.O. Fabritius, A. Ziegler, S. Nikolov, P. Hemzalová, D. Raabe, J. Neugebauer, Ab initio study of single-crystalline and polycrystalline elastic properties of Mg-substituted calcite crystals, J. Mech. Behav. Biomed. Mater. 20 (2013) 296–304. https://doi.org/10.1016/j.jmbbm.2013.01.030.

[38] M.E. Kunitake, L.M. Mangano, J.M. Peloquin, S.P. Baker, L.A. Estroff, Evaluation of strengthening mechanisms in calcite single crystals from mollusk shells, Acta Biomater. 9 (2013) 5353–5359. https://doi.org/10.1016/j.actbio.2012.09.030.

[39] Z. Deng, L. Chen, L. Li, Comparative nanoindentation study of biogenic and geological calcite, J. Mech. Behav. Biomed. Mater. 137 (2023) 105538. https://doi.org/10.1016/j.jmbbm.2022.105538.

[40] S. Khaleghi, F.N. Dehnavi, M. Baghani, M. Safdari, K. Wang, M. Baniassadi, On the directional elastic modulus of the TPMS structures and a novel hybridization method to control anisotropy, Mater. Des. 210 (2021) 110074. https://doi.org/10.1016/j.matdes.2021.110074.

[41] S.I. Ranganathan, M. Ostoja-Starzewski, Universal elastic anisotropy index, Phys. Rev. Lett. 101 (2008) 3–6. https://doi.org/10.1103/PhysRevLett.101.055504.

[42] W.H. Meeks, G. Tinaglia, Triply periodic constant mean curvature surfaces, Adv. Math. (N. Y). 335 (2018) 809–837. https://doi.org/10.1016/j.aim.2018.07.018.

[43] O. Al-Ketan, R.K. Abu Al-Rub, Multifunctional Mechanical Metamaterials Based on Triply Periodic Minimal Surface Lattices, Adv. Eng. Mater. 21 (2019) 1–39. https://doi.org/10.1002/adem.201900524.

[44] T. Yang, Z. Jia, Z. Wu, H. Chen, Z. Deng, L. Chen, Y. Zhu, L. Li, High strength and damage-tolerance in echinoderm stereom as a natural bicontinuous ceramic cellular solid, Nat. Commun. 13 (2022) 6083. https://doi.org/10.1038/s41467-022-33712-z.

[45] A. Berman, L. Addadi, S. Weiner, Interactions of sea-urchin skeleton macromolecules with growing calcite crystals- a study of intracrystalline proteins, Nature. 331 (1988) 546–548. https://doi.org/10.1038/331546a0.

[46] E. Beniash, Spiculogenesis in Sea Urchin Larva, Weizmann Institute of Science, 1998.

[47] A.J.M. Spencer, Continuum Mechanics, Longman Group Limited, London, 1980. http://journal.um-surabaya.ac.id/index.php/JKM/article/view/2203.

[48] P. O'Neill, Structure and mechanics of starfish body wall, J. Exp. Biol. 147 (1989) 53–89. https://doi.org/10.1242/jeb.147.1.53.

[49] L. Schwertmann, O. Focke, J. Dirks, Morphology, shape variation and movement of skeletal elements in starfish (Asterias rubens), J. Anat. 234 (2019) 656–667. https://doi.org/10.1111/joa.12964.

[50] L. Tomholt, L.J. Friesen, D. Berdichevsky, M.C. Fernandes, C. Pierre, R.J. Wood, J.C. Weaver, The structural origins of brittle star arm kinematics: An integrated tomographic, additive manufacturing, and parametric modeling-based approach, J. Struct. Biol. 211 (2020) 107481. https://doi.org/10.1016/j.jsb.2020.107481.

[51] R. Gabbrielli, I.G. Turner, C.R. Bowen, Development of modelling methods for materials to be used as bone substitutes, Key Eng. Mater. 361-363 II (2008) 901–906. https://doi.org/10.4028/www.scientific.net/kem.361-363.903.

[52] S. Vijayavenkataraman, L. Zhang, S. Zhang, J.Y.H. Fuh, W.F. Lu, Triply periodic minimal surfaces sheet scaffolds for tissue engineering applications: An optimization approach toward biomimetic scaffold design, ACS Appl. Bio Mater. 1 (2018) 259–269. https://doi.org/10.1021/acsabm.8b00052.

[53] G. Donnay, D.L. Pawson, X-ray Diffraction Studies of Echinoderm Plates, Science. 166 (1969) 1147–1150. https://doi.org/10.2307/1727473.

[54] J. Aizenberg, J. Hanson, M. Ilan, L. Leiserowitz, T.F. Koetzle, L. Addadi, S. Weiner, Morphogenesis of calcitic sponge spicules: a role for specialized proteins interacting with growing crystals, FASEB J. 9 (1995) 262–268. https://doi.org/10.1096/fasebj.9.2.7781928.

[55] H.A. Lowenstam, S. Weiner, On Biomineralization, Oxford University Press, New York, 1989. https://doi.org/10.1093/oso/9780195049770.001.0001.

[56] E. Beniash, J. Aizenberg, L. Addadi, S. Weiner, Amorphous calcium carbonate transforms into calcite during sea urchin larval spicule growth, Proc. R. Soc. B Biol. Sci. 264 (1997) 461–465. https://doi.org/10.1098/rspb.1997.0066.